Evaluation of 3D Deformation Error Due to Insufficient Observations Using SAR Simulator

Ishii Y.[1*] and Susaki J.[2]

[1] Assistant Professor, Graduate School of Engineering, Kyoto University, Japan

[2] Professor, Graduate School of Engineering, Kyoto University, Japan

*ishii.yoshie.4k@kyoto-u.ac.jp (*Corresponding author's email only)

Abstract *SAR can measure land deformation along line-of-sight direction, and we can estimate three-dimensional surface deformation, using SAR images acquired on ascending and descending orbits, and GNSS observations. However, there is a case that both orbits of SAR images can't be available because SAR images are expensive and even if both orbits of SAR images are acquired, it is not necessarily interfering. Therefore, it is valuable to consider how to effectively use one side orbit SAR images for three-dimensional surface deformation estimation. In order to use effectively one side orbit SAR images in the future, we evaluate the behavior of the error caused by one side orbit SAR images to both side orbit SAR images using SAR simulator in this study. It was supposed to plane as topography and uplift and subsidence deformation. We calculated the subtraction between the deformation estimated by both side orbit SAR images and GNSS interpolation information and the deformation by one side orbit SAR images and GNSS interpolation information to evaluate the error magnitude for each dimension. As a result, the maximum difference of estimated surface deformation between one side orbit SAR images and GNSS and both side orbit SAR images and GNSS are approximately same as the magnitude of deformation. We also examined whether there would be a difference between the estimated surface deformation of one side orbit SAR images and GNSS and both side orbits SAR images and GNSS with and without deformation at the GNSS point, and found that the difference was relatively small. In future work, we will consider how to apply these simulator-based one-side orbit error evaluations to real and more complicated SAR images.*

Keywords: SAR simulator, GNSS, surface deformation, three-dimensional analysis, error evaluation

Introduction

SAR sensors can observe in any weather conditions, day or night, and are characterized by their ability to capture deformation of a few millimeters to a few centimeters by performing interferometric analysis. Therefore, SAR sensors are expected to be used for monitoring and forecasting natural disasters such as landslides (Moretto et al., 2021), earthquakes (Weston et al., 2012), and volcanic eruptions (Schaefer, 2015).

However, acquired SAR images indicate only one dimension, line-of-sight direction ground surface deformation. Therefore, it is not enough to catch accurate ground surface deformation. To solve this problem, several three-dimensional ground surface

deformation estimation methods have been proposed. Fujiwara et al. (2000) proposed a method called 2.5-dimensional analysis. Synthesizing ascending and descending orbit SAR images, the deformation is decomposed into semi east and west and semi uplift and subsidence directions. 2.5-dimensional analysis can analyze the deformation only using SAR images. However, there are strictly several degrees of gaps from east and west direction. In addition, this method assumes the deformation of the north-south direction is zero. Multiaperture InSAR (Interferometry SAR) (MAI) techniques have been proposed to provide the north-south direction of ground surface deformation (Bechor and Zebker, 2006). After that, the fusion of D-InSAR (Differential-InSAR) and MAI measurement is proposed by Jung et al. (2011) for mapping three-dimensional surface deformation. A method for three-dimensional ground surface deformation estimation using a combination of SAR imagery and Global Satellite Navigation System (GNSS) has been proposed by Gudmundsson et al. (2002). Since GNSS is spatially sparse, it is used for spatial interpolation using kriging. GNSS also has the advantage of not being as weakly sensitive to north-south deformation like SAR images. After that, Catalao et al. (2011) suggested the fusion of the results of PS-InSAR (Parmanent Scatter Interferometric SAR) and GPS (Global Positioning System) to estimate the three-dimensional displacement velocities.

For three-dimensional surface deformation estimation, at least three interferometric SAR images observed from at least three different directions are usually required, and at least two images are needed for each interferometric SAR analysis, so at least six SAR images are needed in total. Even if one of the three different observations were to be replaced by GNSS, at least four SAR images would be needed. On the other hand, only a few SAR images may be available in a year if the same SAR sensor, same orbit, same observation mode, and same observation angle for interference are met. If the available interval is too long, SAR images may not interfere with each other. In addition, some SAR images are expensive, and depending on the purpose of the observation, appropriate SAR images may not be available. Thus, sometimes it is difficult to obtain a sufficient number of SAR images for three-dimensional surface deformation analysis.

This study provides an example of how a SAR simulator can be effectively used to address this problem of insufficient SAR images. This study focuses on three-dimensional surface deformation estimation by combining SAR imagery and interpolated GNSS. In three-dimensional surface deformation estimation using SAR images and GNSS, the

number of equations is greater than the number of solutions, so the least-squares method is used for estimation. For better accuracy, it is desirable to have interferometric SAR images for both ascending and descending orbits and interpolated GNSS data, but even if only interferometric SAR images for one side orbit are available, they can be solved from four equations using the least-squares method. However, in general, estimation using one side orbit SAR images is considered to be less accurate than estimation using both side orbits SAR images because the amount of information is reduced. In addition, it is not clear to what extent the estimation results differ between using SAR images of one side orbit and interpolated GNSS and using SAR images of both side orbits and interpolated GNSS. If this difference can be quantitatively clarified, it may be possible to estimate the surface deformation when interferometric SAR images of both side orbits can be estimated by correcting for the case when only one side orbit interferometric SAR images are available.

Therefore, the objective of this study is to quantitatively evaluate the difference between the surface deformation estimated from interferometric SAR images for only one ascending or descending orbit and interpolated GNSS and the surface deformation estimated from interferometric SAR images for both ascending and descending orbits and interpolated GNSS using a SAR simulator developed by Teranishi et al. (2023) and Susaki and Teranishi (2024). In this study, two patterns of GNSS points are assumed: one is to take points from a location with deformation and the other is to take points from a location without deformation.

The remainder of this paper is organized as follows: the Methodology section describes the general structure of the SAR simulator, followed by a detailed description of the processing at each step. In the Results and Discussion section, the simulated surface deformation is evaluated both numerically and visually for the case of one side orbit interferometric SAR imagery and interpolated GNSS and for the case of both side orbits interferometric SAR imagery and interpolated GNSS, and the findings obtained and issues not addressed in this study are discussed. In the Conclusion and Recommendation section, we summarize the study and discuss future prospects.

Methodology

In this study, we use an SAR simulator to assess the accuracy of three-dimensional ground surface deformation estimation. The SAR simulator was constructed by Teranishi et al. (2023) and Susaki and Teranishi (2024). The general flow of the SAR simulator is shown in Figure 1.

a. Making topography and deformation:

In the step of making topography and deformation, we set several conditions. First, the topography was set to Plane. Then, uplift-subsidence deformation was set. The velocity of deformation was set to 0.1 m/year. The location of the deformation was set to $(x, y) = (500, 500)$ and radius $r = 100$.

b. SLC image generation:

In the step of SLC image generation, the information of topography and deformation was read in the simulator. This study assumed Advanced Land Observing Satellite-2 (ALOS-2)/Phased Array type L-band Synthetic Aperture Radar-2 (PALSAR-2) images. Therefore, the wavelength was set to $\lambda = 0.2361$ m. Five SLC images were generated for ascending and descending orbit, respectively. The heading angle was set to 0 degrees and the observation direction was right.

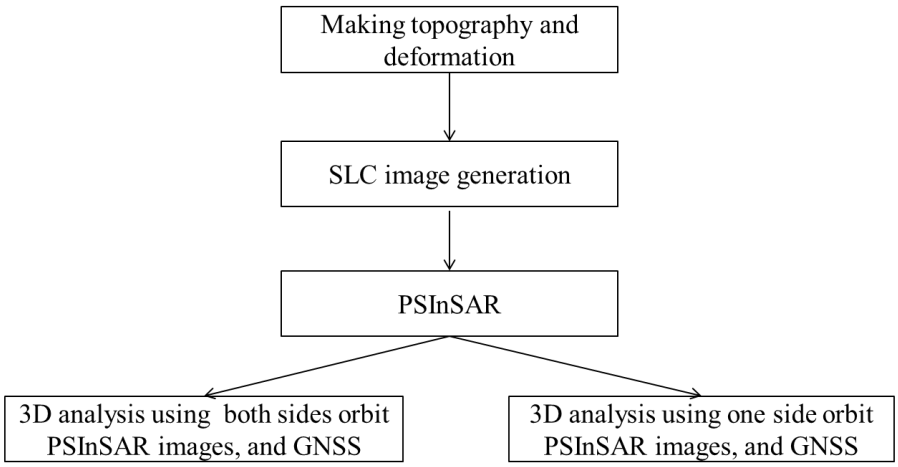

Figure 1: Flow of the SAR simulator used in this study

c. PSInSAR:

In the step of PSInSAR (Permanent Scatter Interferometric SAR), we estimated the average surface deformation velocity from five SLC images using Permanent Scatter (PS)

points (Ferretti, 2001). Master image is selected based on the following equation (Kampes, 2006).

Where,

$$\min\left(\frac{1}{N-1}\sum_{k=0}^{N-1} g\left(B_{\perp}^{k,m}, a_1\right)\cdot g\left(T^{k,m}, a_2\right)\right) \quad (1)$$

$$g(x,a)=\begin{cases} 1-\dfrac{|x|}{a} & \text{if } |x|<a \\ 0 \text{ otherwize} \end{cases}$$

Here, N is total number of images, m is master image, k is slave image. $B_{\perp}^{k,m}$ and $T^{k,m}$ are vertical baseline length and time baseline length between m-th and k-th SAR images, respectively. a_1 and a_2 are critical vertical baseline length and critical time baseline length, respectively.

Using the following equations, the average surface deformation velocity and Digital Elevation Model (DEM) error that maximizes the absolute value of time coherence γ are calculated.

$$\text{argmax}\left(|\gamma|=\left|\frac{1}{N}\sum_{k=1}^{N}\exp\left\{i\left(\Delta\varphi_{Flat}-\varphi_{Defo}-\varphi_{TopoErr}\right)\right\}\right|\right) \quad (2)$$

Where,

$$\varphi_{Defo}=\frac{4\pi}{\lambda}T_k\cdot v, \qquad \varphi_{TopoErr}=\frac{4\pi}{\lambda}\frac{B_{\perp}^{k,m}}{R}\left(\frac{1}{\sin\theta}+1\right)\Delta h$$

Here, $\Delta\varphi_{Flat}$ is the phase difference component of the interferometry image, in which the effects of baseline length and DEM were removed. φ_{Defo} and $\varphi_{TopoErr}$ are phase changes caused by the surface deformation and DEM errors. T_k is time difference from the master

image. v is the average surface deformation velocity. Δh is DEM error. θ is off-nadir angle.

d. Three-dimensional deformation estimation:

After the generation of PSInSAR images, three-dimensional deformation estimation was conducted. The deformation velocity of line-of-sight (LOS) is expressed as follows.

$$\begin{aligned} V_{LOS}^{ASC} &= \cos\phi_{ASC} \sin\theta_{ASC} V_e + \sin\phi_{ASC} \sin\theta_{ASC} V_n + \cos\theta_{ASC} V_u \\ &= u_e^{ASC} V_e + u_n^{ASC} V_n + u_u^{ASC} V_u \end{aligned} \quad (3)$$

$$\begin{aligned} V_{LOS}^{DES} &= \cos\phi_{DES} \sin\theta_{DES} V_e + \sin\phi_{DES} \sin\theta_{DES} V_n + \cos\theta_{DES} V_u \\ &= u_e^{ASC} V_e + u_n^{ASC} V_n + u_u^{ASC} V_u \end{aligned} \quad (4)$$

Here, ASC is Ascending orbit and DES is Descending orbit. ϕ is the heading angle of the satellite and θ is the incident angle of the radar. V_e, V_n, V_u are the velocity of east-west, north-south, and uplift-subsidence, respectively. u_e, u_n, u_u are the unit vectors pointing from the PS toward the satellite.

In this study, we use the GNSS information which is spatially interpolated using the kriging method. The velocity interpolated by GNSS are expressed as $V_e^{GNSS}, V_n^{GNSS}, V_u^{GNSS}$.

From ascending orbit LOS velocity and GNSS velocity, the following equation is constructed.

$$\begin{bmatrix} V_{LOS}^{ASC} \\ V_e^{GNSS} \\ V_n^{GNSS} \\ V_u^{GNSS} \end{bmatrix} = \begin{bmatrix} u_e^{ASC} & u_n^{ASC} & u_u^{ASC} \\ 1 & 0 & 0 \\ 0 & 1 & 0 \\ 0 & 0 & 1 \end{bmatrix} \begin{bmatrix} V_e \\ V_n \\ V_u \end{bmatrix} \quad (5)$$

Similarly, from descending orbit LOS velocity and GNSS velocity, the following equation is constructed.

$$\begin{bmatrix} V_{LOS}^{DES} \\ V_e^{GNSS} \\ V_n^{GNSS} \\ V_u^{GNSS} \end{bmatrix} = \begin{bmatrix} u_e^{DES} & u_n^{DES} & u_u^{DES} \\ 1 & 0 & 0 \\ 0 & 1 & 0 \\ 0 & 0 & 1 \end{bmatrix} \begin{bmatrix} V_e \\ V_n \\ V_u \end{bmatrix} \quad (6)$$

In addition, from both orbit LOS velocity and GNSS velocity, the following equation is constructed.

$$\begin{bmatrix} V_{LOS}^{ASC} \\ V_{LOS}^{DES} \\ V_e^{GNSS} \\ V_n^{GNSS} \\ V_u^{GNSS} \end{bmatrix} = \begin{bmatrix} u_e^{ASC} & u_n^{ASC} & u_u^{ASC} \\ u_e^{DES} & u_n^{DES} & u_u^{DES} \\ 1 & 0 & 0 \\ 0 & 1 & 0 \\ 0 & 0 & 1 \end{bmatrix} \begin{bmatrix} V_e \\ V_n \\ V_u \end{bmatrix} \tag{7}$$

Here, the above matrixes and vectors are described as follows.

$$A = \begin{bmatrix} u_e^{ASC} & u_n^{ASC} & u_u^{ASC} \\ 1 & 0 & 0 \\ 0 & 1 & 0 \\ 0 & 0 & 1 \end{bmatrix}, \quad B = \begin{bmatrix} u_e^{DES} & u_n^{DES} & u_u^{DES} \\ 1 & 0 & 0 \\ 0 & 1 & 0 \\ 0 & 0 & 1 \end{bmatrix},$$

$$C = \begin{bmatrix} u_e^{ASC} & u_n^{ASC} & u_u^{ASC} \\ u_e^{DES} & u_n^{DES} & u_u^{DES} \\ 1 & 0 & 0 \\ 0 & 1 & 0 \\ 0 & 0 & 1 \end{bmatrix},$$

$$V_{obs}^{ASC} = \begin{bmatrix} V_{LOS}^{ASC} \\ V_e^{GNSS} \\ V_n^{GNSS} \\ V_u^{GNSS} \end{bmatrix}, \quad V_{obs}^{DES} = \begin{bmatrix} V_{LOS}^{DES} \\ V_e^{GNSS} \\ V_n^{GNSS} \\ V_u^{GNSS} \end{bmatrix}, \quad V_{obs}^{BOTH} = \begin{bmatrix} V_{LOS}^{ASC} \\ V_{LOS}^{DES} \\ V_e^{GNSS} \\ V_n^{GNSS} \\ V_u^{GNSS} \end{bmatrix}, \quad V_{defo} = \begin{bmatrix} V_e \\ V_n \\ V_u \end{bmatrix}$$

Using the least squares method, three-dimensional deformations are estimated as follows.

$$\hat{V}_{defo}^{ASC} = (A^T A)^{-1} A^T V_{obs}^{ASC} \tag{8}$$

$$\hat{V}_{defo}^{DES} = (B^T B)^{-1} B^T V_{obs}^{DES} \tag{9}$$

$$\hat{V}_{defo}^{BOTH} = (C^T C)^{-1} C^T V_{obs}^{BOTH} \tag{10}$$

The objective of this study is to assess the difference of estimated three-dimensional deformation between one side orbit and two side orbit. Therefore, the subtraction and RMSE between $\hat{V}_{defo}^{ASC}$ and $\hat{V}_{defo}^{BOTH}$, $\hat{V}_{defo}^{DES}$ and $\hat{V}_{defo}^{BOTH}$, $\hat{V}_{defo}^{ASC}$ and $\hat{V}_{defo}^{DES}$ are calculated.

Results and Discussion:

Figure 2 indicates the given up-down velocity and the simulated LOS velocity on ascending and descending orbits. The positive value means uplift, and the negative value means subsidence.

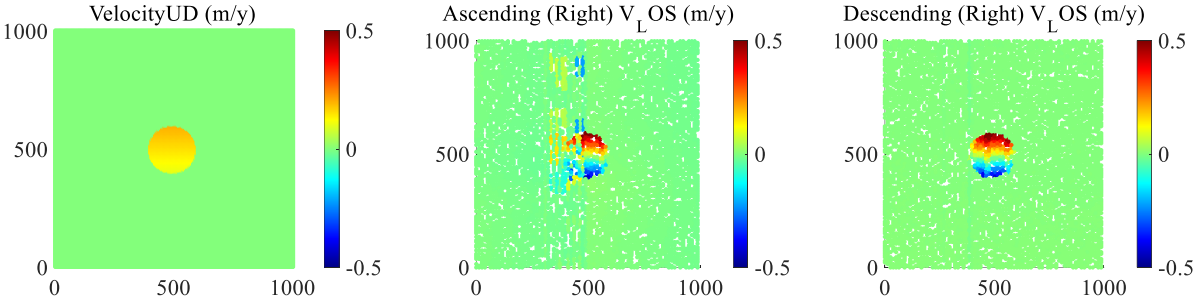

(a) Actual up-down velocity (m/y) (b) Ascending LOS velocity (m/y) (c) Descending LOS velocity (m/y)

Figure 2: Actual velocity and simulated LOS velocity

Figure 3 shows the results of the deformation estimation under the condition that up-down deformation is assumed and GNSS velocity is zero. Figure 3 (a1), (a2) and (a3) show the given deformation velocity, and the pink points indicate the location of GNSS. Figure 3 (b1), (b2) and (b3) show the interpolated velocity based on GNSS points. Figure 3 (c1), (c2) and (c3) show the estimated by SAR images on ascending orbit and GNSS. The estimated up-down velocity is variated from negative to positive values. In addition, the estimated east-west velocity is also variated from negative to positive values although the actual velocity is zero. The velocities estimated by SAR images on descending orbit and GNSS in Figure 3 (d1), (d2) and (d3) and by SAR images on ascending and descending orbits and GNSS in Figure 3 (e1), (e2) and (e3) indicate similar trends with Figure 3 (c1), (c2) and (c3).

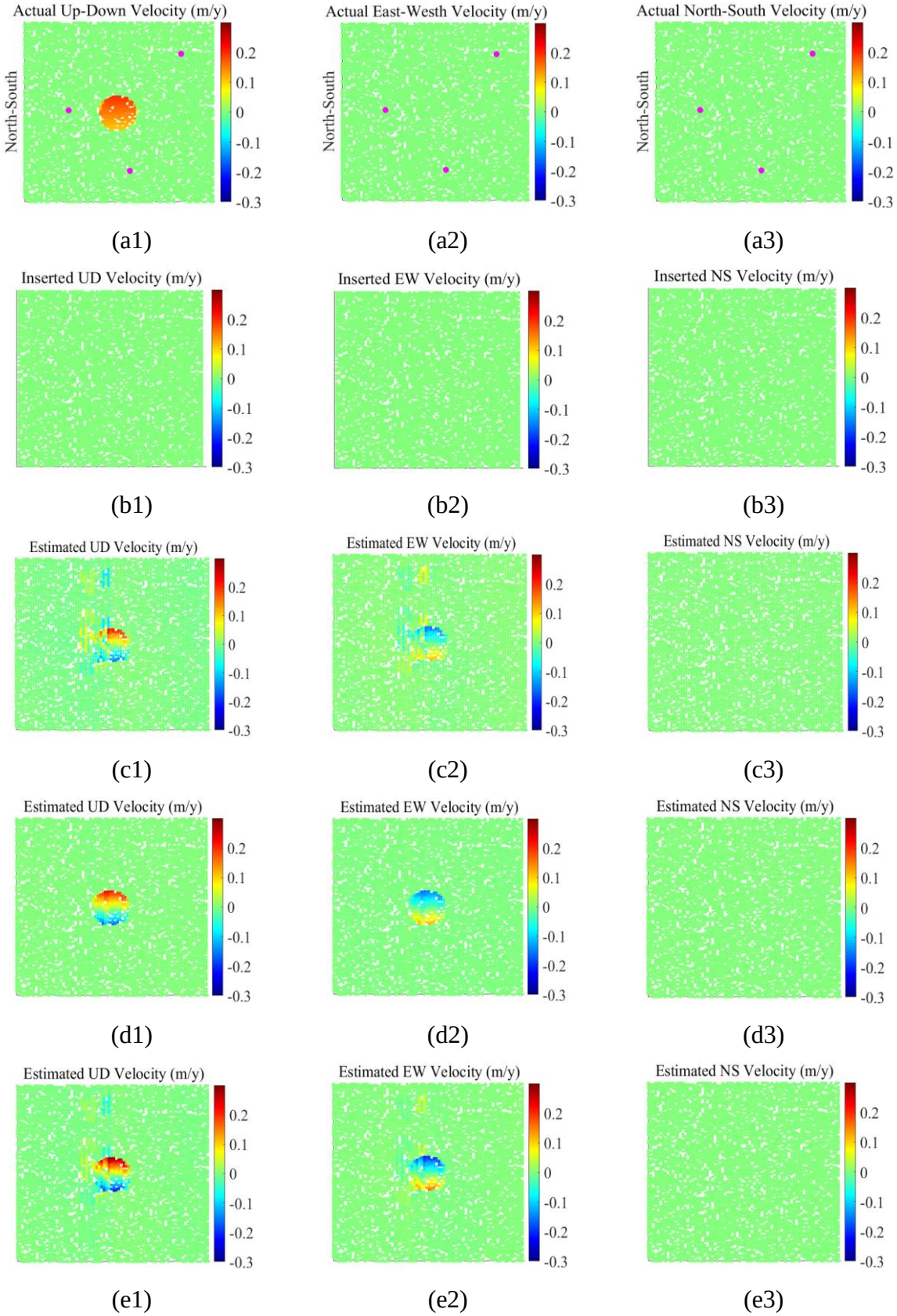

Figure 3: Estimation of deformation under the condition that up-down deformation is assumed and GNSS velocity was zero.

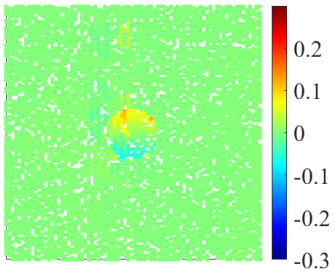

(a) Difference between ASC+DES+GNSS and ASC+GNSS (UD)

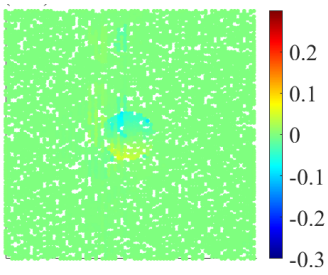

(b) Difference between ASC+DES+GNSS and ASC+GNSS (EW)

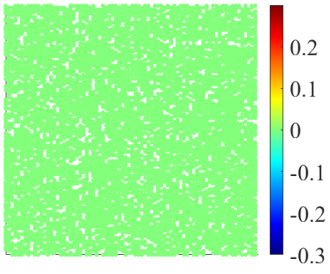

(c) Difference between ASC+DES+GNSS and ASC+GNSS (NS)

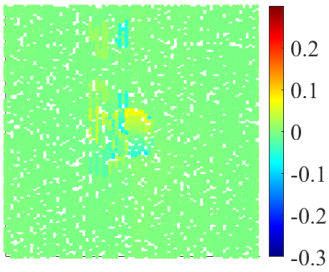

(d) Difference between ASC+DES+GNSS and DES+GNSS (UD)

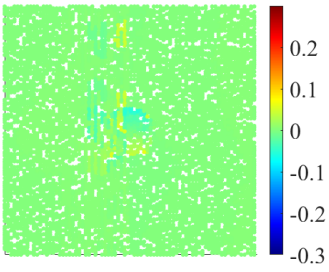

(e) Difference between ASC+DES+GNSS and DES+GNSS (EW)

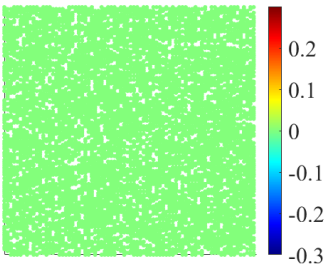

(f) Difference between ASC+DES+GNSS and DES+GNSS (NS)

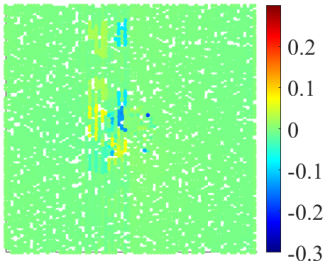

(g) Difference between ASC+GNSS and DES+GNSS (UD)

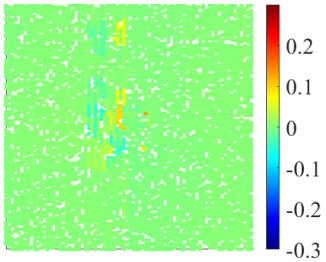

(h) Difference between ASC+GNSS and DES+GNSS (EW)

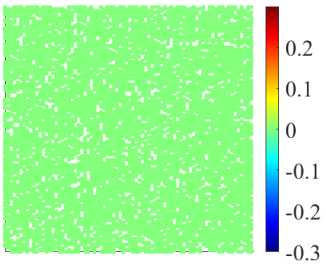

(i) Difference between ASC+GNSS and DES+GNSS (NS)

Figure 4: Subtraction of estimated deformation velocity [m/y] between SAR images on different orbit under the condition that up-down deformation is assumed and GNSS velocity was zero

Figure 4 shows the results of subtraction of estimated deformation velocity [m/y] between SAR images on different orbit under the condition that up-down deformation is assumed and GNSS velocity was not zero. In Figure 4, larger absolute values mean that the effect of differences in the data used for deformation estimation is larger.

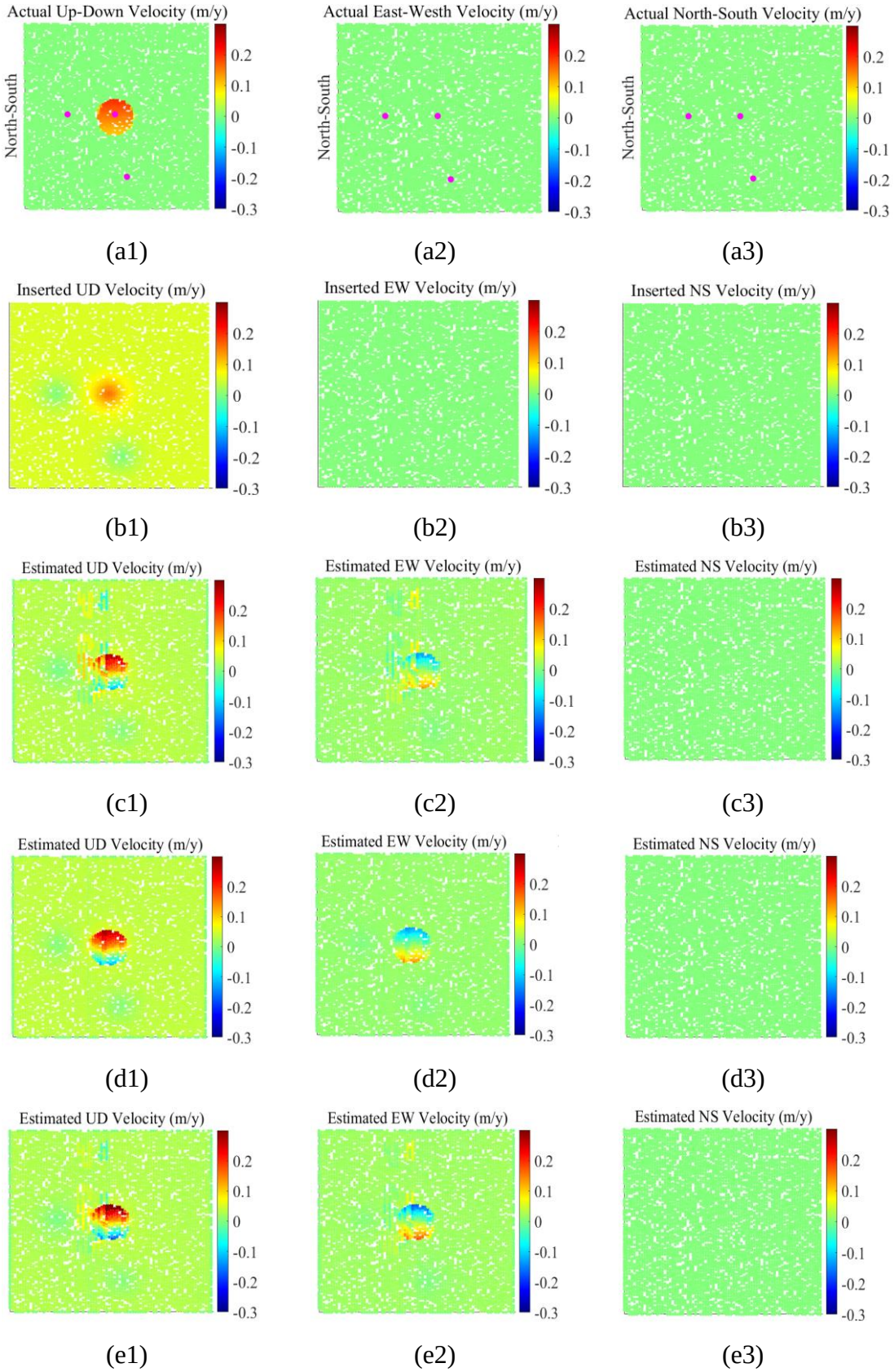

Figure 5: Estimation of deformation under the condition that up-down deformation is assumed and GNSS velocity was not zero.

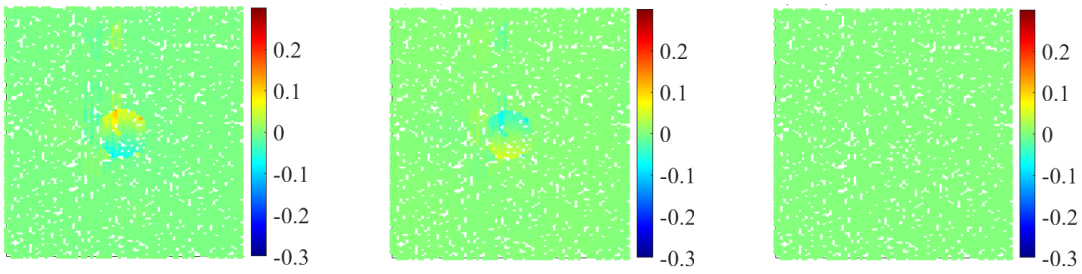

(a) Difference between ASC+DES+GNSS and ASC+GNSS (UD)

(b) Difference between ASC+DES+GNSS and ASC+GNSS (EW)

(c) Difference between ASC+DES+GNSS and ASC+GNSS (NS)

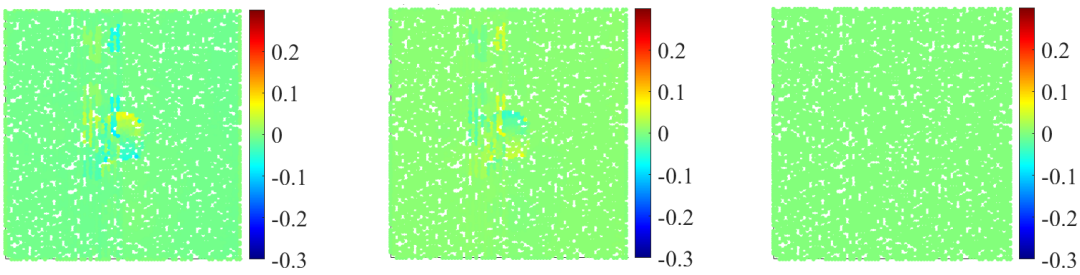

(d) Difference between ASC+DES+GNSS and DES+GNSS (UD)

(e) Difference between ASC+DES+GNSS and DES+GNSS (EW)

(f) Difference between ASC+DES+GNSS and DES+GNSS (NS)

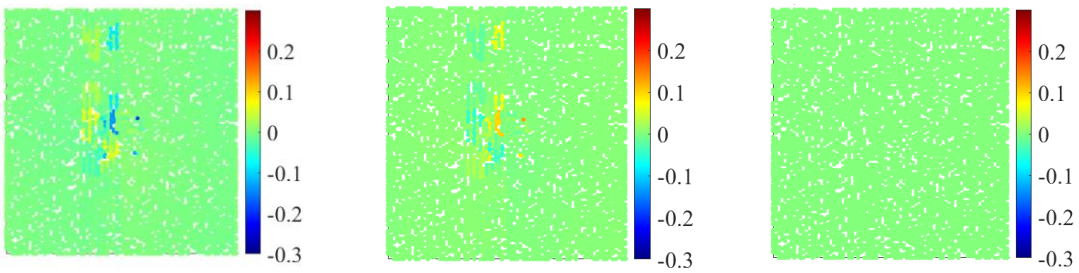

(g) Difference between ASC+GNSS and DES+GNSS (UD)

(h) Difference between ASC+GNSS and DES+GNSS (EW)

(i) Difference between ASC+GNSS and DES+GNSS (NS)

Figure 6: Subtraction of estimated deformation velocity [m/y] between different SAR orbit images under the condition that up-down deformation is assumed and GNSS velocity was not zero.

Figure 4 (a), (b) and (c) show the difference of velocity between SAR images on ascending and descending orbits and GNSS and SAR images on ascending orbit and GNSS. It was confirmed that where the amount of deformation velocity was larger, the impact of the difference in data used was also larger. Figure 4 (d), (e) and (f) indicate

similar results to Figure 4 (a), (b) and (c) but are noisier. This noise is considered to be generated in the step of SLC image generation.

Figure 5 shows the results of the deformation estimation under the condition that up-down deformation is assumed and GNSS velocity was not zero. As the results of including the GNSS point which has velocity, the entire image has velocity as shown in Figure 5 (c1), (c2), (d1), (d2), (e1) and (e2).

Figure 6 shows the results of the subtraction of estimated deformation velocity [m/y] between SAR images on different orbit under the condition that up-down deformation is assumed and GNSS velocity was not zero. We found that the trends of velocity difference caused by the difference of used SAR data in Figure 6 are similar to Figure 4.

In order to assess quantitatively, we calculated the maximum and minimum values and RMSE of the velocity difference as shown in Table 1. “No deformation” in the second column in Table 1 corresponds to Figure 4. “Include deformation” in the second column in Table 1 corresponds to Figure 6. In the results of “ASC+DES+GNSS vs ASC+GNSS”, the maximum difference in up-down deformation direction was 0.128 [m/y] under the condition that GNSS was “No deformation”, and the maximum difference in up-down deformation direction was 0.118 [m/y] under the condition that GNSS was “Include deformation.” In the results of “ASC+DES+GNSS vs DES+GNSS”, the maximum difference in up-down deformation direction was 0.076 [m/y] under the condition that GNSS was “No deformation“, and the maximum difference in up-down deformation direction was 0.066 [m/y] under the condition that GNSS was “Include deformation.” The reason that the maximum values in the up-down deformation direction in “ASC+DES+GNSS vs ASC+GNSS” is larger than that in “ASC+DES+GNSS vs DES+GNSS” is considered to be noise arose at the step of SLC image generation. These results imply that the maximum difference in estimated velocity between one side orbit and both side orbits becomes the same magnitude as the actual deformation velocity. The same conclusion can be drawn for the minimum difference because that value is considered to be the maximum difference by taking absolute values. On the other hand, the difference of the east-west deformation, which is not actually occurring, between one side orbit and both side orbits is not as large as that of the up-down deformation. This is a

reasonable result because we can consider that the smaller the original value is, the smaller the difference value is.

Then, we discuss the presence or absence of deformation velocity at GNSS points. The difference between “No deformation” and “Include deformation” was at most 0.01. This value is one-tenth of the difference in deformation velocity between one side orbit and both side orbits. This means the influence of GNSS velocity on the difference between one side orbit and both side orbits is relatively small.

Table 1: Quantitative assessment [m/y]

Comparison data	GNSS	Up-Down			East-West			North-South		
		Max	Min	RMSE	Max	Min	RMSE	Max	Min	RMSE
ASC+DES +GNSS vs ASC +GNSS	No deformation (Fig.3)	0.128	-0.073	0.009	0.052	-0.091	0.006	0.000	0.000	0.000
	Include deformation (Fig. 4)	0.118	-0.080	0.009	0.058	-0.085	0.006	0.000	0.000	0.000
	Subtraction	0.010	0.008	0.000	-0.005	-0.007	0.000	0.000	0.000	0.000
ASC+DES +GNSS vs DES+GNSS	No deformation (Fig. 3)	0.076	-0.083	0.009	0.059	-0.055	0.007	0.000	0.000	0.000
	Include deformation (Fig. 4)	0.066	-0.090	0.012	0.064	-0.047	0.008	0.000	0.000	0.000
	Subtraction	0.010	0.007	-0.003	-0.005	-0.007	-0.002	0.000	0.000	0.000
ASC +GNSS vs DES +GNSS	No deformation (Fig. 3)	0.077	-0.186	0.013	0.133	-0.055	0.010	0.000	0.000	0.000
	Include deformation (Fig. 4)	0.077	-0.186	0.013	0.133	-0.055	0.010	0.000	0.000	0.000
	Subtraction	0.000	0.000	0.000	0.000	0.000	0.000	0.000	0.000	0.000

Finally, we discuss future challenges and possibilities. In this experiment, we assessed the difference of estimated deformation velocity focused on up-down direction. Therefore, it is also necessary to assess the difference of estimated deformation velocity focused on east-west and north-south directions because there is the possibility indicating different trends. In addition, this experiment targeted plane topography. However, the topography is complex in the real world. Also, the influence of topography is considered to be large for the difference of estimated deformation between one side orbit and both side orbits. Therefore, it is necessary to simulate various topography started from simple slope topography to complex topography. The purpose of simple topography is to capture the universal and essential features. On the other hand, the purpose of complex topography is to reproduce the world close to reality. If the relationship between the difference in estimated deformation for one side orbit and both side orbits for various terrain types can

be clarified, it may be possible to estimate the deformation for both side orbits when the SAR image for one orbit is only available. And, although we set only the deformation velocity of 0.1 m/year in this experiment, it is necessary to assess the difference of deformation velocity between one side orbit and both side orbits under the conditions of the several deformation velocities. Because it does not clarify that the difference of deformation between one side orbit and both side orbits equals to the magnitude of the actual deformation velocity as shown in this study.

Conclusion and Recommendation

Today, SAR sensors are expected to be used for monitoring and forecasting natural disasters such as landslides, earthquake, and volcanic eruptions. Because SAR images can be observed in all weather conditions and day and night. However, they are expensive, and the number of images obtained is small considering interference conditions and other factors. In addition, SAR images of the same orbit capture only line-of-sight (LOS) deformation, and estimating three-dimensional deformations requires SAR images of at least three orbits or supplementary data such as GNSS.

The objective of this study was to quantitatively evaluate the effect of the number of orbits of SAR images and the presence or absence of GNSS deformation velocity in the estimation of three-dimensional deformation by combining SAR imagery and GNSS interpolation data using a SAR simulator. This study targeted the up-down surface deformation in the plane. From the experiments using SAR simulator, it was found that the maximum difference of estimated surface deformation velocity was approximately same as the given surface deformation velocity. In addition, it is clear that the difference between the surface deformation velocity estimated by SAR imagery for one side orbit and GNSS and the surface deformation velocity estimated by SAR imagery and GNSS for both side orbits is relatively small, comparing GNSS includes local deformation and does not include local deformation.

On the other hand, the experiments conducted in this study were under very limited conditions and further experiments are needed. Therefore, conditions that should be considered in the future are summarized below. First, it is necessary to check whether the same results can be obtained when the surface deformation occur in the east-west and north-south directions. In particular, different results may be obtained for the north-south

direction because of the weak sensitivity of SAR to the direction of travel. Second, it is necessary to study the situation on a variety of topography other than flat surfaces. Especially in terrain with many inclines, such as mountainous terrain, the areas that can be observed in ascending and descending orbits may be very different. In such cases, the results of estimating the surface deformation by one side orbit SAR images and by both side orbit SAR images may also be significantly affected. Third, this study only considered the case of the surface deformation velocity 0.1 m/year, but did not discuss the case of different surface deformation velocities. Therefore, the effects of varying the deformation velocity should also be investigated. Finally, we will clarify the correspondence between the estimation of surface deformation from one side orbit SAR images and that from both side orbit SAR images based on experiments under these various conditions, and develop a method to obtain more accurate surface deformation by correcting for the case where only one side orbit SAR images are available.

Founding

This work was supported by the AY2024 TOYOTARIKEN scholar.

References

Bechor, N. B., & Zebker, H. A. (2006). Measuring two-dimensional movements using a single InSAR pair. *Geophysical research letters*, 33(16).

Catalão, J., Nico, G., Hanssen, R., & Catita, C. (2011). Merging GPS and atmospherically corrected InSAR data to map 3-D terrain displacement velocity. *IEEE Transactions on Geoscience and Remote Sensing*, *49*(6), 2354-2360.

Ferretti, A., & Rocca, F. (2001). Permanent scatterers in SAR interferometry. *IEEE Transactions on Geoscience and Remote Sensing, 39 (1), 8-20,* doi: 10.1109/36.898661.

Fujiwara, S., Nishimura, T., Murakami, M., Nakagawa, H., Tobita, M., & Rosen, P. A. (2000). 2.5-D surface deformation of M6. 1 earthquake near Mt Iwate detected by SAR interferometry. *Geophysical research letters*, *27*(14), 2049-2052.

Gudmundsson, S., Sigmundsson, F., & Carstensen, J. M. (2002). Three-dimensional surface motion maps estimated from combined interferometric synthetic aperture radar and GPS data. *Journal of Geophysical Research: Solid Earth*, *107*(B10), ETG-13.

Jung, H. S., Lu, Z., Won, J. S., Poland, M. P., & Miklius, A. (2010). Mapping three-dimensional surface deformation by combining multiple-aperture interferometry and conventional interferometry: Application to the June 2007 eruption of Kilauea volcano, Hawaii. *IEEE Geoscience and Remote Sensing Letters*, *8*(1), 34-38.

Kampes, B. M. (2006). The permanent scatterer technique. *Radar interferometry: Persistent Scatterer Technique*, 5-30.

Moretto, S., Francesca B., & Paolo M. (2021). The role of satellite InSAR for landslide forecasting: limitations and openings, *Remote Sensing*, 13 (18), 3735. https://doi.org/10.3390/rs13183735

Schaefer, L. N., Lu, Z., & Oommen, T. (2015). Dramatic volcanic instability revealed by InSAR. *Geology*, *43*(8), 743-746.

Susaki, J., & Teranishi, Y. (2024). Unbiased estimation of three-dimensional deformation from SAR interferometry and GNSS observations, *IEEE Journal of Selected Topics in Applied Earth Observations and Remote Sensing*, 17, 5761-5773, doi: 10.1109/JSTARS.2024.3365545.

Teranishi,Y., Ishii,Y., Susaki, J., Hisada, H., & Oba, T. (2023). Development and application of pseudo-SAR image simulator, *2023 8th Asia-Pacific Conference on Synthetic Aperture Radar (APSAR), Bali, Indonesia*, 1-5, doi: 10.1109/APSAR58496.2023.10388621.

Weston, J., Ferreira, A. M., & Funning, G. J. (2012). Systematic comparisons of earthquake source models determined using InSAR and seismic data. *Tectonophysics*, *532*, 61-81.